

A multispectral microscope for *in vivo* oximetry of rat dorsal spinal cord vasculature

Marieke A van der Putten¹, Lewis E MacKenzie^{1,2}, Andrew L Davies³, Javier Fernandez-Ramos¹, Roshni A Desai³, Kenneth J Smith³ and Andrew R Harvey¹

¹ School of Physics and Astronomy, University of Glasgow, Glasgow, United Kingdom

² School of Biomedical Sciences, University of Leeds, Leeds, United Kingdom

³ Department of Neuroinflammation, University College London Institute of Neurology, London, United Kingdom

Email: Andy.Harvey@Glasgow.ac.uk

Abstract

Quantification of blood oxygen saturation (SO₂) *in vivo* is essential for understanding the pathogenesis of diseases in which hypoxia is thought to play a role, including inflammatory disorders such as multiple sclerosis (MS) and rheumatoid arthritis (RA). We describe a low-cost multispectral microscope and oximetry technique for calibration-free absolute oximetry of surgically exposed blood vessels *in vivo*. We imaged the vasculature of the dorsal spinal cord in healthy rats, and varied inspired oxygen (FiO₂) in order to evaluate the sensitivity of the imaging system to changes in SO₂. The venous SO₂ was calculated as 67.8 ± 10.4% (average ± standard deviation), increasing to 83.1 ± 11.6% under hyperoxic conditions (100% FiO₂) and returning to 67.4 ± 10.9% for a second normoxic period; the venous SO₂ was 50.9 ± 15.5% and 29.2 ± 24.6% during subsequent hypoxic states (18% and 15% FiO₂ respectively). We discuss the design and performance of our multispectral imaging system, and the future scope for extending this oximetry technique to quantification of hypoxia in inflamed tissue.

Keywords: multispectral imaging, oximetry, spinal cord vasculature

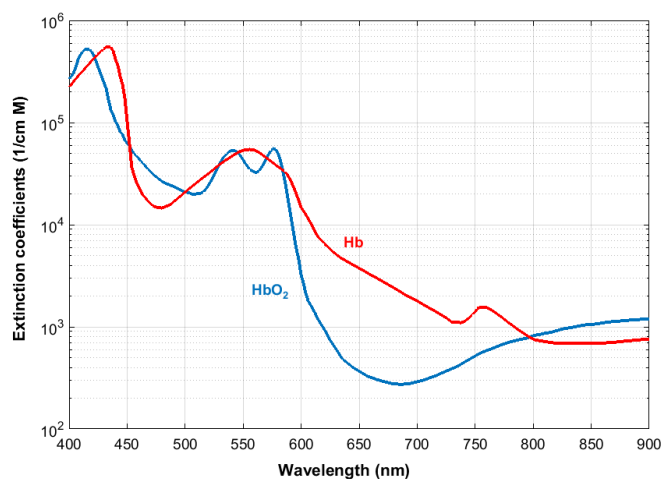
1. Introduction

Tissue hypoxia is associated with inflammation in a range of diseases (Eltzschig & Carmeliet, 2011), including rheumatoid arthritis (RA) (Taylor & Sivakumar, 2005), and inflammation of the central nervous system such as occurs in multiple sclerosis (MS) (Davies, et al., 2013) (Desai, et al., 2016). Measurement of blood oxygen saturation in the vasculature can provide valuable information as to the oxygenation state of the tissue (Beach, 2014). Multispectral imaging (MSI) has become established as a method for vascular oximetry, with a diverse variety of *in vivo* applications including non-invasive retinal oximetry (Mordant, et al., 2011; Choudhary, et al., 2013), ocular microvascular oximetry (MacKenzie, et al., 2016), and investigation of tumour hypoxia in mouse models (Sorg, et al., 2005). The principle of MSI vascular oximetry is based upon the oxygen-dependent optical absorption of haemoglobin, which is the dominant absorber of light in blood. Figure 1 shows the molar extinction coefficients of oxygenated and deoxygenated haemoglobin (values from Prahl, 1999). Unlike techniques for tissue oximetry such as Near-Infrared Spectroscopy (NIRS) which use diffuse transmission measurements through tissue (Murkin & Arango, 2009), in vascular oximetry blood vessels are imaged directly. It is thus possible with vascular oximetry to obtain oxygen saturation

48 measurements localised to individual blood vessels – something that is not possible with other oximetric
 49 techniques such as NIRS.

50 Vascular oximetry using MSI involves estimation of the absorbance of blood vessels at various
 51 oxygen-insensitive (isosbestic) and oxygen-sensitive wavelengths. The optical density of a blood vessel
 52 can be empirically related to SO_2 , provided there are known reference values for *in vivo* blood
 53 oxygenation, obtained through prior calibration (e.g. two-wavelength oximetry in the retina (Beach, et
 54 al., 1999)). Unfortunately, for many applications where localised oximetry *in vivo* is desirable, there are
 55 no known reference values as the local environment is highly variable. Absolute calibration-free
 56 oximetry may be achieved however, by determining transmission of light through a blood vessel,
 57 imaged at multiple wavebands, and fitting the measured transmission values to a theoretical optical
 58 model. The model we employ here is based upon the modified Beer-Lambert law, and includes optical
 59 absorption, scattering, and other parameters. In this study we applied a multispectral oximetry
 60 algorithm which builds upon previous work by others, predominantly for retinal oximetry (Schweitzer,
 61 et al., 1995) (Smith, et al., 2000). In addition, we introduce a new contrast-reduction parameter to
 62 account for losses of contrast, which can be caused by minor amounts of tissue overlying blood vessels
 63 and neighbouring tissue (see Section 2.3). It also compensates for loss of image contrast caused by the
 64 modulation transfer function of the imaging system.

65



66

67 **Figure 1.** Molar extinction coefficients of oxygenated (HbO₂) and deoxygenated haemoglobin (Hb) as
 68 a function of wavelength (Prahl, 1999).

69 To date, the SO_2 dynamics of the rat spinal cord dorsal veins have not been thoroughly
 70 investigated, with only a few limited studies conducted. Figley et al. (2013) reported use of a
 71 commercial two-wavelength photoacoustic tomography (PAT) imaging system to monitor a temporary
 72 decrease of the dorsal vein SO_2 in rats during hypoxia, however the method for calibration of the PAT
 73 device is not reported. Lesage et al. (2009) and Sharma et al. (2011) studied the use of optical imaging
 74 and non-imaging light-reflectance spectroscopy respectively, to monitor changes in concentration of
 75 oxyhaemoglobin in the rat spinal cord in response to electrical stimulation. Absolute SO_2 values were
 76 not reported, however.

77 Here we introduce a multispectral imaging system suitable for *in vivo* oximetry, and a
 78 complementary multispectral oximetry algorithm. The imaging system was designed and assembled
 79 using low cost, off-the-shelf optical components. We present results of measurement of venous SO_2 in
 80 the dorsal spinal cord vasculature of anaesthetised healthy control rats during normoxia (21% fraction
 81 of inspired oxygen [FiO_2]), hyperoxia (100% FiO_2), and hypoxia (18% and 15% FiO_2). This is an easily

82 transferable technique, and we believe the approach presented in this paper could be applied to the *in*
83 *vivo* study of a variety of experimental models in which hypoxia is thought to play a role.

84

85

86 **2. Methods**

87

88 *2.1. Multispectral microscope*

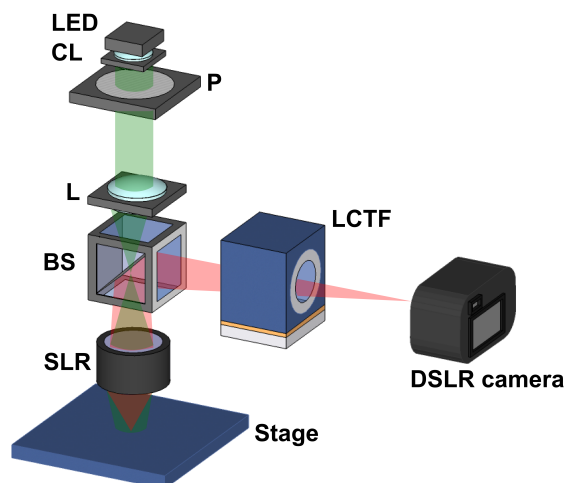
89 A schematic of the multispectral microscope is displayed in Figure 2. The microscope was designed
90 such that the back focal length of the objective allowed sufficient working space for access to the
91 exposed spinal cord of a rat under general anaesthesia. The microscope also enabled room for surgical
92 equipment and was portable so as to be transferred between labs if necessary. A low-magnification,
93 wide field-of-view system was implemented enabling oximetry of blood vessels across a range of
94 diameters, and multispectral images between 546 nm and 600 nm were acquired.

95 Illumination was provided by a white LED (*MWWHL3*, *Thorlabs*) with a collimator lens of focal length
96 40.0 mm (*COP-5A*, *Thorlabs*). An additional lens (*LA1509*, *Thorlabs*, $f = 100$ mm) served as a
97 condenser lens for the illumination path. The LED was controlled by a 4-channel driver (*DC4100*,
98 *Thorlabs*). A liquid crystal tuneable filter (LCTF) (*VIS-7-HC-20*, *Varispec*) provided electronically-
99 controllable spectral discrimination in 1 nm steps between 400 and 700 nm, with spectral full-width at
100 half maximum of 8 nm. Orthogonal polarisation imaging was used to null specular reflections from
101 blood vessels. In consequence the intensity profile obtained from images of the blood vessels arises
102 from light that has been depolarised by multiple scattering within the spinal cord and blood vessels. The
103 analysis described in section 2.2 therefore neglects specularly reflected light, using the ratio of the light
104 intensity either side of the blood vessel to the intensity at the centre of the vessel to estimate Beer-
105 Lambert law attenuation of light transmitted through the blood vessel. This polarisation configuration
106 was achieved by placing a linear polariser (*LPVISE200-A*, *Thorlabs*) in the illumination path oriented
107 to be orthogonal to the polarisation axis of the LCTF.

108 A single lens reflex (SLR) served as the microscope objective (AF Nikkor f/1.8, $f = 50$ mm),
109 and was configured for finite conjugate imaging. The position of the SLR lens could be manually
110 translated along the z-axis for adjustment of focus. A digital SLR camera (*D300s*, *Nikon*) was used as
111 the detector.

112 Images were saved as 14-bit RGB NEF (RAW) format and converted to uncompressed
113 greyscale TIFF images for analysis. Greyscale conversion involved selecting either the red or the green
114 channel of the sensor and subtracting the respective dark current channel. The choice of red or green
115 channel was made for each waveband based on which provided higher SNR at that waveband; the red
116 channel was used for $580 \leq \lambda \leq 600$ nm, and the green channel for $546 \leq \lambda \leq 570$ nm. Image acquisition
117 rate was limited by the USB camera interface, which transferred RAW images at a rate of one image
118 every 7.5 seconds; thus a 6-band multispectral dataset was acquired in approximately 45 seconds total.
119 The SLR CMOS detector had 4288 x 2800 pixels and was 23.6 mm by 15.8 mm. The field of view of
120 this configuration was approximately 3.69 mm by 2.47 mm, giving a magnification factor of 6.4
121 corresponding to 0.88 μm per pixel. Automated control of illumination, spectral filtering, and image
122 acquisition was achieved using a custom LabVIEW interface.

123



124
 125 **Figure 2.** Schematic of multispectral microscope. LED: light emitting diode; CL: collimating lens; P:
 126 linear polariser; L: condenser lens; BS: beamsplitter; LCTF: liquid crystal tuneable filter; SLR lens is
 127 oriented with back focal plane towards the target. The illumination path is shown in green, and the
 128 imaging path in red.

129
 130 *2.2. Multispectral image processing and determination of optical transmission*

131 Six wavebands were selected for imaging: 546, 560, 570, 584, 590 and 600 nm. Sensitivity to changes
 132 in SO₂ was provided by the 560 nm, 590 nm and 600 nm wavebands. The 546 nm, 570 nm and 584 nm
 133 wavebands were isosbestic, i.e. their absorptions are oxygen-insensitive (see Figure 1). These
 134 wavebands provided close to optimal transmission for oximetry in vessels approximately 100 μm in
 135 diameter. Accurate oximetry is possible for 0.1 < T < 0.7 (Smith, 1999), where T is the proportional
 136 transmission of light propagated through the blood vessel. Wavelengths longer than 600 nm
 137 are unsuitable, as light of this wavelength is weakly absorbed by oxygenated haemoglobin, resulting in
 138 low contrast and hence sub-optimal transmission for accurate oximetry. For example, illumination of a
 139 100 μm blood vessel at 700 nm results in optical transmission values of 0.71 and 0.68 for oxygenated
 140 and deoxygenated haemoglobin respectively (as calculated using the beer-lambert law), which
 141 illustrates the poor contrast between oxygenation states at this wavelength. Wavelengths below 546 nm
 142 have poor signal-to-noise ratio due to the low intensity of the LED and the low transmission of the
 143 LCTF at these wavelengths, and as such were also deemed unsuitable.

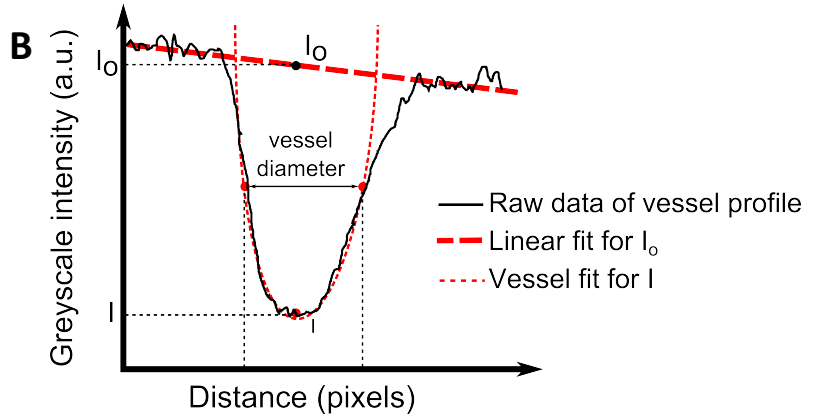
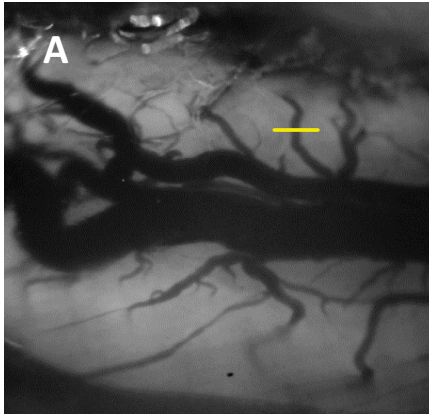
144 All image processing was implemented using custom algorithms in MATLAB. Images at each
 145 waveband were co-registered to form a 6-waveband multispectral data-cube. Vessels were tracked
 146 semi-automatically using user-defined control points. A vessel-profile fitting algorithm (see Figure 3)
 147 was used to estimate vessel diameter at each waveband at each point along the veins. Diameter
 148 estimation was based on the technique described by Fischer et al. (2000); this algorithm determines
 149 edges of the vessel as the points of greatest gradient in the 546 nm line profile. From this, the diameter
 150 of a vessel in pixels, and hence diameter in microns, could be determined. Transmission of vessels at
 151 each wavelength was then determined by a second vessel fitting algorithm. To estimate background
 152 intensity (I_o), a linear fit (the red dashed line in Figure 3B) was applied to points of the line profile
 153 adjacent to the vessel. A second-order polynomial was fitted to the profile inside the vessel to estimate
 154 the intensity at the centre of the vessel (I) (the black dashed line, Figure 3B). The transmission (T) of
 155 the vessel was then calculated by $T = \left(\frac{I}{I_o}\right)$.

156

157 Only vessels meeting the following inclusion criteria were selected for tracking and oximetry analysis:

- 158 1. Vessels with diameter between 50 and 130 μm .
 159 2. Vessels producing a transverse line profile at least three times their diameter, and free of any
 160 adjacent vessels, to avoid systemic error in optical transmission calculation.
 161 3. Vessels without taper - e.g. due to curvature around the spinal cord tissue.

162 Typically only one or two vessels per rat met these inclusion criteria.
 163



164 **Figure 3.** (A) Schematic of line profile along a spinal cord vessel – many such line profiles are taken
 165 along each vessel for analysis. (B) Illustration of vessel fitting algorithm used determine vessel diameter
 166 and estimate transmission of light at each waveband. 2.3. Oximetry algorithm

168 A multispectral oximetry algorithm based on the work of Smith et al. (2000) was developed to estimate
 169 SO_2 from transmission values of blood vessels. This algorithm fits a theoretical model of vessel
 170 transmission to experimentally measured transmission values, yielding an estimation of SO_2 and related
 171 optical parameters. The original model was validated by comparison to femoral artery blood-gas
 172 measurements in swine (Smith et al, 2000). The theoretical model predicts the wavelength-dependent
 173 transmission of a blood vessel of known diameter by accounting for blood oxygen saturation and
 174 incorporating empirical values for extinction and reduced scattering coefficients reported in the
 175 literature (Prahl, 1999; Faber et al., 2004; Bosschaart et al., 2014). Further, we add an extra “contrast
 176 reduction” parameter– to compensate for local, minor variations in tissue thickness overlying vessels.
 177 This tissue tends to add a scattering component which reduces vessel contrast and hence transmission
 178 values, leading to incorrect estimation of SO_2 . This section briefly describes how the model was derived.

179 From the Beer-Lambert law of optical transmission and absorption, we first defined the optical
 180 density (OD) of a blood vessel as:

$$181 \quad OD = \log_{10}(T) = \varepsilon(\lambda)C_{HbT}d, \quad (1)$$

182 where $T \left(T = \frac{I}{I_0} \right)$ is the experimentally measured transmission of a vessel as depicted in Fig. 3, d is the
 183 vessel diameter, C_{HbT} is the molar concentration of total haemoglobin, and $\varepsilon(\lambda)$ is the effective optical
 184 extinction coefficient of haemoglobin; $\varepsilon(\lambda)$ is dependent on both the oxygen saturation and
 185 wavelength-dependent molar extinction coefficients $\varepsilon_{HbO_2}(\lambda)$ and $\varepsilon_{Hb}(\lambda)$ of oxygenated and
 186 deoxygenated haemoglobin respectively. The ratio T is in essence an estimate of the ratio of the light
 187 transmitted through the blood vessel to the intensity of light that would have been scattered from the
 188 location of the vessel centre in the absence of the vessel. This ratio is thus insensitive to variations in
 189 source spectral intensity and the precise optical characteristics of the spinal cord. As discussed below,
 190

191 the light intensity at the centre of the vessel is due to two dominant components: single-pass light arising
 192 from light that has diffused laterally to back illuminate the blood vessel and a double-pass component
 193 light that is transmitted through the vessel, scattered from the spinal cord and reflected back through
 194 the vessel. A third component due to direct back scatter from the vascular blood is insignificant at these
 195 wavelengths and can be neglected. When this technique is used in the retina the presence of variable
 196 amounts of pigment (melanin, retinal pigment) means that the relative magnitudes of these components
 197 vary within and between retinas. Due to the low level of pigmentation in the spinal cord it is expected
 198 that the single-pass transmission is dominant (the tissue point-spread function is much larger than the
 199 diameter of the blood vessel) and there should be low variability between and within spinal cords.
 200 We used accepted values from the literature shown in Figure 1 (Prahl, 1999). These values are derived
 201 from human blood, but it has been shown that the difference between the absorption of light by
 202 haemoglobin in rats and humans is minimal (Zijlstra, et al., 1994). Defining c_1 and c_2 as proportional
 203 concentrations of oxygenated (HbO₂) and deoxygenated (Hb) haemoglobin respectively, (1) is rewritten
 204 as

$$OD = (\varepsilon_{HbO_2}(\lambda) c_1 + \varepsilon_{Hb}(\lambda) c_2) d \quad (2)$$

206 where: $c_1 + c_2 = C_{HbT}$, so $c_1 = C_{HbT}SO_2$ and $c_2 = C_{HbT}(1 - SO_2)$, and SO_2 is the oxygen saturation; in other
 207 words, the proportion of oxygenated haemoglobin in the total solution of haemoglobin. It was also
 208 necessary to introduce a parameter to account for attenuation due to optical scattering by blood.
 209 Equation (2) is thus rewritten as:

$$OD = C_{HbT}d \left[(\varepsilon_{HbO_2}(\lambda) - \varepsilon_{Hb}(\lambda)) SO_2 + \varepsilon_{Hb}(\lambda) \right] + \mu'(\lambda)d \quad (3)$$

211 where the $\mu'(\lambda)$ is the wavelength-dependent reduced scattering coefficient, which considers
 212 wavelength-dependent scattering (Faber, et al., 2004). By using compiled average values of scattering
 213 coefficients $\mu(\lambda)$ and scattering anisotropy factors $g(\lambda)$, we determined these reduced scattering
 214 coefficients: $\mu'(\lambda) = \mu(\lambda)(1 - g(\lambda))$ (Bosschaart, et al., 2014).

215 Two parameters, α and β , are also introduced to account for the combination of single-pass
 216 transmission and double-pass transmission as described above. This concept is based on Smith, et al.,
 217 (2000) and was further validated by Monte Carlo modelling in Hammer et al. (2001) and Rodmell et al.
 218 (2014). There will also be a component of transmission which results from direct back-scattering of
 219 incident light from the vessel surface, however we omit this due to our illumination configuration
 220 employing crossed polarisers. Equation (3) is then rewritten in terms of transmission as:

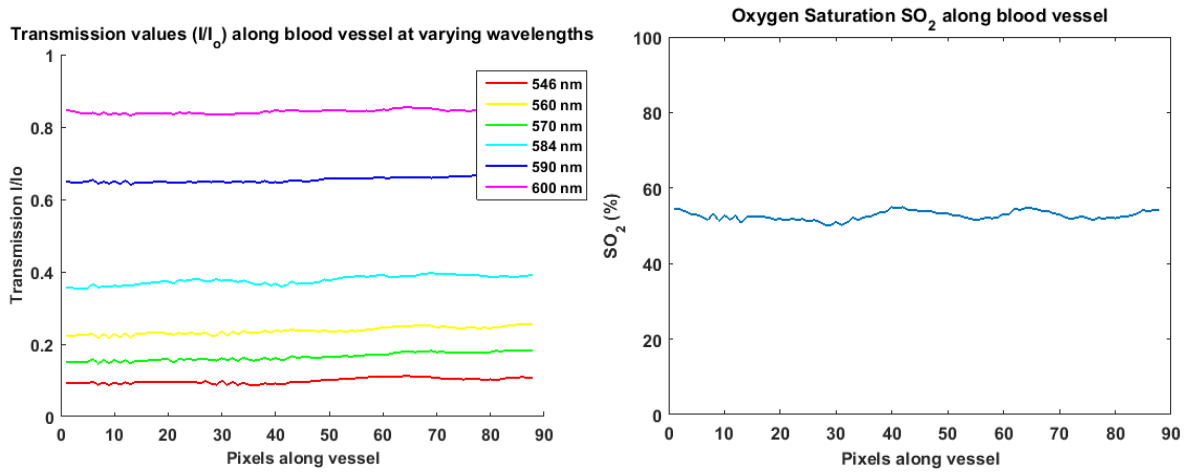
$$T(\lambda) = \left(\alpha 10^{-\left(C_{HbT} d \left[(\varepsilon_{HbO_2}(\lambda) - \varepsilon_{Hb}(\lambda)) SO_2 + \varepsilon_{Hb}(\lambda) \right] + \mu'(\lambda) d \right)} \right. \\ \left. + \beta 10^{-\left(2 C_{HbT} d \left[(\varepsilon_{HbO_2}(\lambda) - \varepsilon_{Hb}(\lambda)) SO_2 + \varepsilon_{Hb}(\lambda) \right] + 2 \mu'(\lambda) d \right)} \right) \quad (4)$$

223 Finally, it was considered that various factors other than SO_2 may alter the measured
 224 transmission values, such as scattering by overlying tissue. The imaging system itself may also
 225 introduce scattering and hence a loss of contrast. Contrast reduction was incorporated as an increase in
 226 greyscale intensity I_c of both the background and the vessel. Transmission was hence re-defined as
 227 $T'(\lambda) = \left(\frac{I + I_c}{I_o + I_c} \right)$. A contrast parameter K was introduced such that $K = \frac{I_c}{I_o + I_c}$. By substitution, this
 228 yields: $T'(\lambda) = T(\lambda)(1 - K) + K$. Applying this substitution to (4), a final model for transmission was
 229 derived:

230

$$T'(\lambda) = \left(\alpha 10^{-\left(C_{HbT}(\lambda)d \left[\left(\epsilon_{HbO_2}(\lambda) - \epsilon_{Hb}(\lambda) \right) SO_2 + \epsilon_{Hb}(\lambda) \right] + \mu'(\lambda)d \right)} + \beta 10^{-\left(2C_{HbT}(\lambda)d \left[\left(\epsilon_{HbO_2}(\lambda) - \epsilon_{Hb}(\lambda) \right) SO_2 + \epsilon_{Hb}(\lambda) \right] + 2\mu'(\lambda)d \right)} \right) (1 - K) + K. \quad (5)$$

231 The experimentally measured transmissions (obtained as detailed in section 2.2) are then fitted
 232 to the theoretical model of light transmissions (Eq. (5)) using a nonlinear least-squares fit, yielding
 233 estimations of free parameters α , β , K , and SO_2 . A trust region reflective algorithm was employed to
 234 perform this least-squares fit. Additionally, vessel diameter was allowed to vary from the measured
 235 vessel diameter by $\pm 5 \mu m$. Similarly to SO_2 , the optical parameters α , β and K are all assumed to be
 236 invariant over the $\sim 55 \text{ nm}$ waveband range employed in the illumination scheme. The resulting fits were
 237 robust, with SO_2 approximately constant along the vessel. Figure 4 presents an illustrative example of
 238 experimentally obtained transmissions along a blood vessel at all six wavebands, and the resulting SO_2
 239 values along the vessel, as produced by the algorithm.
 240



241
 242 **Figure 4.** (A) Example of transmission profile along a tributary vessel. (B) SO_2 estimated by the
 243 multispectral oximetry algorithm along the same vessel.

244
 245 *2.4. In vivo imaging procedure*

246 All procedures involving animals were carried out in accordance with the ARRIVE guidelines and the
 247 United Kingdom Home Office Animals (Scientific Procedures) Act 1986. Four female Dark Agouti rats
 248 (average weight 180 g) were used for the control validation study. A laminectomy was performed under
 249 2% isoflurane anaesthesia in room air, and the dorsal aspect of vertebral segment L1 was removed to
 250 expose the cord for imaging. After surgery, the isoflurane was reduced to 1.5% for the remainder of the
 251 experiment, including all imaging. Motion due to animal heart-beat and breathing can provide a
 252 challenge for *in vivo* imaging, but surgical sutures were used to reduce loading of weight on the rat
 253 ribcage and the spinous process rostral to the exposed cord was clamped in place using a modified
 254 hemostatic clamp, minimising motion sufficiently for imaging. Similar strategies have been employed
 255 in other studies which imaged the murine spinal cord (Johannssen & Helmchen, 2010), (Vinegoni, et
 256 al., 2014), (Cadotte, et al., 2012).

257 Arterial SO_2 was monitored and recorded throughout the experiment using a pulse-oximeter
 258 collar (MouseOx, STARR Life). A homeothermic heating mat and rectal temperature probe maintained
 259 the rectal temperature at $37^\circ C$. For each rat, image exposure time for each waveband was optimised to
 260 ensure sufficient exposure and to avoid image saturation.

261 Assessing changes in SO_2 due to changes in FiO_2 is an effective and established method for testing the
262 sensitivity of the oximetry technique (Yi, et al., 2015). To assess response to changes in FiO_2 in healthy
263 rats, FiO_2 was varied sequentially, with three full multispectral datasets acquired at each stage of the
264 experiment. The following sequence was used: baseline normoxia (21% FiO_2 for 10 minutes),
265 hyperoxia (100% FiO_2 for 10 minutes), return to normoxia (normoxia 2, 21% FiO_2 for 5 minutes), then
266 incrementally decreasing FiO_2 to induce progressive hypoxia (hypoxia 1, 18% and hypoxia 2, 15%; 5
267 minutes each). Similar protocols have been used in previous oximetry studies (MacKenzie, et al., 2016),
268 and have been shown to produce a sequence of SO_2 changes that is clearly distinct from normal
269 physiological variation.

270

271

272

273 **3. Results**

274

275 *3.1. Images acquired*

276 Multispectral images were successfully acquired at baseline normoxia 1, hyperoxia, normoxia 2, and
277 hypoxia 1 for all four rats. Rat 1 died before the hypoxia 2 oxygenation state (15% FiO_2), and thus
278 hypoxia 2 data are omitted for this rat. Representative multispectral images of rat spinal cord dorsal
279 vein are shown in Figure 5. The large dorsal vein lies on the dorsal surface of the spinal cord along the
280 rostral-caudal axis, with numerous smaller tributary veins. The large dorsal vein is too absorbing for
281 accurate oximetry, so tributary veins were analysed, provided they met the inclusion criteria described
282 in Section 2.2.

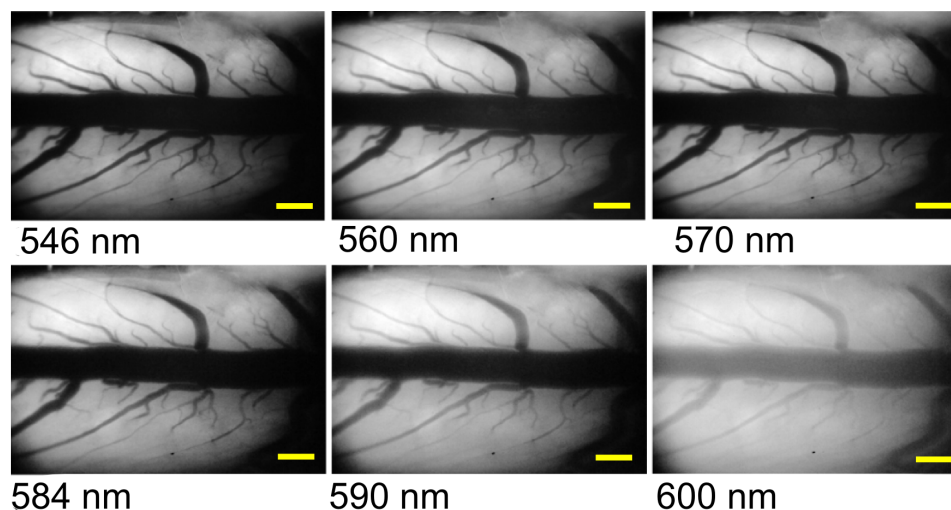
283

284 *3.2. Response to changes in FiO_2*

285 Average venous SO_2 values are shown in Figure 6. Corresponding arterial values, as measured by the
286 pulse oximeter, are also presented. As expected, average baseline venous SO_2 increased during
287 hyperoxia ($67.8 \pm 10.4\%$ [mean \pm standard deviation] increasing to $83.1 \pm 11.6\%$), and returned to
288 baseline values during the second state of normoxia ($67.4 \pm 10.9\%$) and further decreased during
289 subsequent hypoxic periods ($50.9 \pm 15.5\%$ and $29.2 \pm 24.6\%$ respectively). The differences in average
290 SO_2 between consecutive oxygenation states were all statistically significant ($p < 0.05$, pairwise t-test),
291 with changes between normoxia 1 and hyperoxia, hyperoxia and normoxia 2, and normoxia 2 and
292 hypoxia 1 all highly significant ($p < 0.01$). The normoxia baseline SO_2 values and changes due to FiO_2
293 interventions are physiologically plausible (normal venous SO_2 is typically $\sim 70\%$), helping to validate
294 our multispectral oximetry algorithm. The results for venous SO_2 for all individual animals are shown
295 in Figure 7 and Table 1. Vessel diameter measurements for all animals are summarised in Table 2,
296 including results of a pairwise t-test between all diameter values at consecutive oxygenation states –
297 which suggested no relationship between measured SO_2 and vessel calibre.

298

299



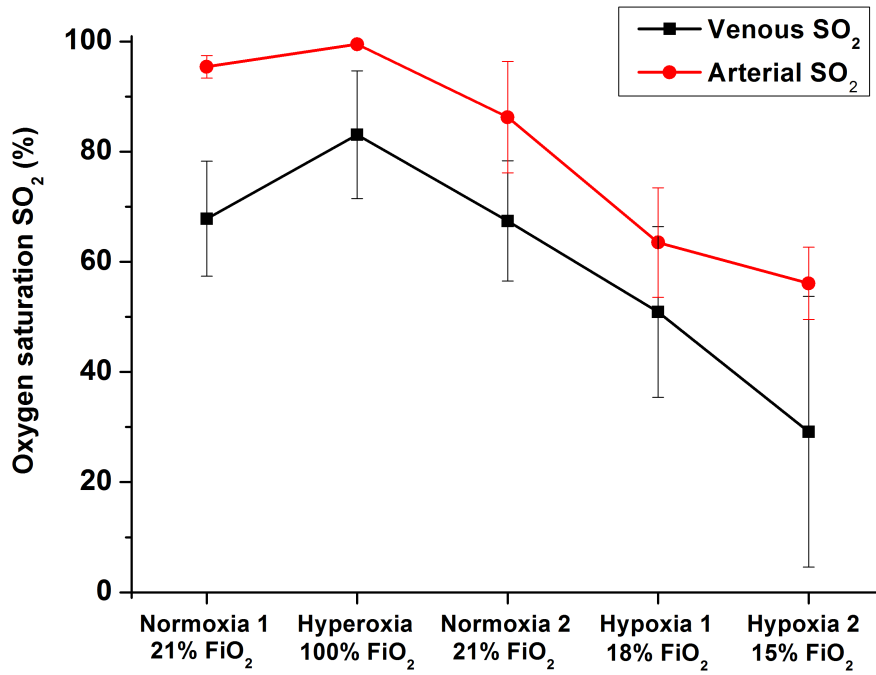
300
301 **Figure 5.** Multispectral images of spinal cord dorsal vein vasculature in a single rat. The main dorsal
302 vein lies on the dorsal surface of the spinal cord, with numerous tributary veins joining the larger vessel.
303 The scale bars represent 500 μm .

304 *3.3. Repeatability and inter-animal variability of measurements*

305 Repeatability of measurements was assessed by performing three measurements of SO_2 at baseline
306 normoxia for each individual rat, where physiological variations are expected to be minimal. The
307 average standard deviation of repeat measurements across all animals was $\pm 2.28\%$ SO_2 . This deviation
308 is much lower than changes in SO_2 observed due to variation of FiO_2 – which was above 15% between
309 normoxia and hyperoxia, and even greater for changes between normoxia and subsequent states of
310 hypoxia. This indicated sufficient repeatability over individual vessels for ascertaining changes in SO_2 .

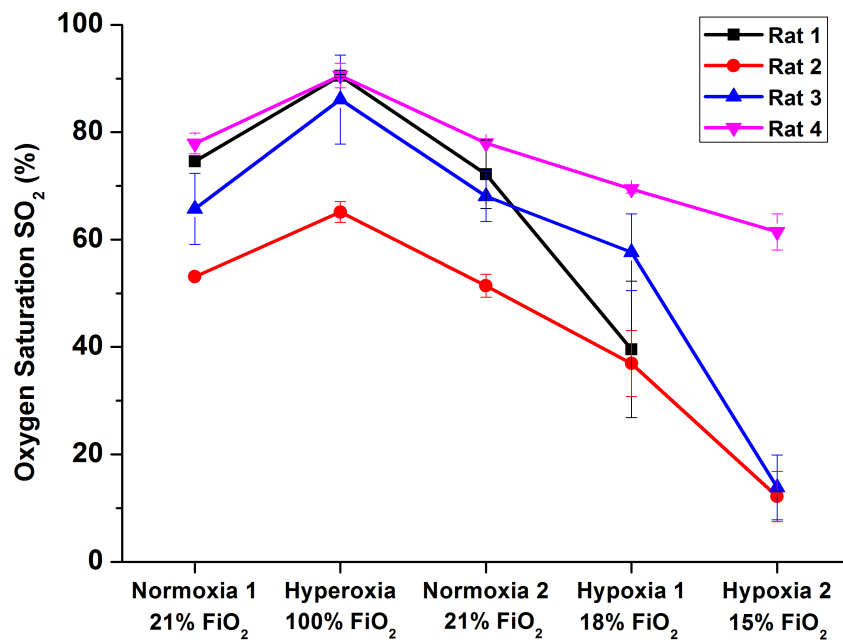
311 The changes in venous SO_2 observed throughout the experiment were strongly correlated with
312 changes in arterial SO_2 , as measured by the pulse oximeter. The calculated Pearson correlation
313 coefficients r were 0.74, 0.79, 0.87, and 0.88 for each rat respectively ($p < 0.01$). There was, however,
314 considerable variation in average baseline venous SO_2 between individual rats, ranging from 53% to
315 78% at normoxia. We did not find a correlation between this variation in venous SO_2 and the baseline
316 arterial SO_2 values. Some physiological variation is expected between rats due to potential differences
317 in depth of anaesthesia and the temperature of the exposed spinal cord (despite maintenance of rectal
318 temperature), both of which may affect venous oxygen saturation.

319



320
321
322
323
324
325
326

Figure 6. Average venous SO₂ across all animals with variation in FiO₂. Corresponding average pulse oximeter data are also presented. Error bars represent the standard deviation of the average values of each individual rat.



327
328
329

Figure 7. Variation in SO₂ with FiO₂ for each control rat. Results are the average value for each rat ± standard deviation.

330 **Table 1.** SO₂ measurements for individual control rats.

Average rat SO₂ ± standard deviation (%)

	Rat 1	Rat 2	Rat 3	Rat 4	Average	Change (p-value)
Normoxia 1 (21% FiO ₂)	74.6 ± 0.1	53.1 ± 0.5	65.8 ± 6.6	77.9 ± 1.9	67.8 ± 10.4	n/a
Hyperoxia (100% FiO ₂)	90.5 ± 0.3	65.2 ± 1.93	86.1 ± 8.3	90.6 ± 2.3	83.1 ± 11.6	<0.01
Normoxia 2 (21% FiO ₂)	72.2 ± 6.4	51.4 ± 2.1	68.1 ± 4.7	78.0 ± 0.2	67.4 ± 10.9	<0.01
Hypoxia 1 (18% FiO ₂)	39.6 ± 12.7	36.9 ± 6.2	57.7 ± 7.2	69.4 ± 0.7	50.9 ± 15.5	<0.01
Hypoxia 2 (15% FiO ₂)	N/A	12.2 ± 4.7	13.8 ± 6.00	61.5 ± 3.4	29.2 ± 24.6	<0.05

331
332
333
334
335
336
337

Table 2. Vessel diameter measurements throughout the experiment.

	Average vessel diameter ± standard deviation (µm)				Change (p-value)
	Rat 1	Rat 2	Rat 3	Rat 4	
Normoxia 1 (21% FiO ₂)	104.5 ± 0.9	87.7 ± 0.6	59.5 ± 1.4	100.5 ± 1.1	n/a
Hyperoxia (100% FiO ₂)	108.1 ± 0.6	89.8 ± 1.8	59.3 ± 1.4	103.0 ± 3.3	0.89
Normoxia 2 (21% FiO ₂)	105.5 ± 1.6	87.6 ± 0.7	57.9 ± 5.00	97.7 ± 1.3	0.81
Hypoxia 1 (18% FiO ₂)	107.0 ± 0.7	86.0 ± 0.7	60.8 ± 1.7	99.4 ± 1.4	0.88
Hypoxia 2 (15% FiO ₂)	N/A	81.7 ± 0.6	61.7 ± 1.3	99.3 ± 0.2	0.34

338
339
340
341
342
343
344
345
346
347
348
349
350

4. Discussion

4.1. Performance of the multispectral microscope

The multispectral microscope provided images of the dorsal vasculature of the rat spinal cord with sufficient magnification and spectral contrast for oximetry of vessels approximately 50 to 130 µm in diameter. Data acquisition was fully automated using a LabVIEW interface to minimise acquisition time and potential human error. Further, the multispectral microscope was assembled with off-the-shelf components, making it a relatively simple and cost-effective device. Using a digital SLR CMOS detector was cost-efficient in comparison with scientific CCD or CMOS detectors, and provided sufficient performance. Further reduction in cost could be achieved by replacing the LCTF with a bank of bandpass filters. The LCTF has the advantage of rapid tuning and adaptability, but LCTF

351 transmission is low and it is the most costly component of the microscope. A computer-controlled filter
352 wheel would result in slower switching between wavebands, but this would be compensated by shorter
353 integration times afforded by higher optical throughput.

354 Integration time was less than 1 second for all wavelengths; for the 584 nm, 590 nm and 600
355 nm wavebands where LCTF transmission is higher, the integration time was as low as 100 ms.
356 Multispectral dataset acquisition rate was limited, however, by the LabVIEW SLR camera control
357 toolbox used (LabVIEW Camera Control for Nikon SLR, *Ackerman Automation*). The resulting data-
358 transfer speed was limited by the USB 2.0 capability of the SLR camera, which limited image
359 acquisition to once every 7.5 seconds. This resulted in an acquisition time of approximately 45 seconds
360 for a multispectral dataset. Acquisition time could be greatly improved in future by using a SLR camera
361 with USB 3.0 capability.

362

363 4.2. Performance and validation of oximetry algorithm for *in vivo* imaging

364 Our oximetry algorithm is based on an algorithm published by Smith et al. (2000). Smith's algorithm
365 was validated in swine by comparing estimations of SO₂ with objective SO₂ measurements obtained by
366 blood-gas analysis of arterial blood from the femoral artery. Further, we have incorporated empirical
367 values of scattering coefficient, anisotropy factor, and extinction coefficients of oxygenated and
368 deoxygenated haemoglobin from the literature, and introduced a novel contrast-reduction parameter to
369 compensate for the optical effects of overlying tissue. Vessel diameter may influence other parameters
370 in our algorithm, such as degree of optical scattering and optical path length of light. In two-wavelength
371 oximetry, for example, it has been reported that large retinal veins are estimated to have a lower blood
372 oxygen saturation than smaller veins (Hammer, et al., 2008), but this may be a vein-diameter dependent
373 calibration artefact in two-wavelength oximetry. We found that fluctuations in diameter for a given
374 vessel between consecutive oxygenation states were not statistically significant (see Table 2), giving
375 confidence that our estimation of SO₂ is independent of blood vessel diameter.

376 It is clear from measurement that our oximetry analysis provides physiologically plausible
377 values for SO₂, is sensitive to changes in SO₂, and is insensitive to vessel diameter. However, highly
378 accurate validation of our oximetry algorithm remains challenging *in vivo*. Whilst the correlations with
379 arterial pulse oximeter data go some way towards explaining the variability in baseline venous SO₂,
380 verifying the absolute values produced by our technique is difficult. An option for an *in vitro* validation
381 study is to use whole *ex vivo* blood in transparent fluorinated ethylene propylene (FEP) capillaries,
382 placed on a diffuse white reflective background material such as SpectralonTM. *In vitro* validation
383 requires variation of SO₂ in blood, generally achieved by addition of measured quantities of sodium
384 dithionite (Briely-Sabo & Bjornerud, 2000). However, sodium dithionite alters the osmolarity of blood
385 which affects optical properties, including scattering coefficients and anisotropy (Friebel, et al., 2010).
386 The development of a more realistic phantom and an alternative method to artificially deoxygenate
387 whole blood, such as the use of nitrogen gas, would be beneficial and will be considered for future
388 studies (Ghassemi, et al., 2015) (Denninghoff & Smith, 2000).

389 Many tributary vessels present in the images were too small (< 50 µm) to meet our inclusion
390 criteria: such vessels absorb light too weakly for accurate oximetry with the wavelengths used. To
391 enable analysis of smaller vessels, blue wavelengths (at which absorption is higher) could be
392 incorporated into the imaging scheme, providing sufficient contrast for accurate determination of
393 transmission profiles. This would increase the number of veins appropriate for analysis.

394

395 5. Conclusions

396

397 We have developed a cost-effective multispectral microscope to enable *in vivo*, calibration-free,
398 absolute oximetry of surgically-exposed dorsal veins of healthy rats. SO₂ and vessel diameters of
399 tributary dorsal veins were calculated for a range of inspired oxygen concentrations. This algorithm
400 yielded physiologically plausible values for SO₂ for each rat during normoxia, hyperoxia and graded
401 hypoxia, with SO₂ changing as expected. Further, these results correlated significantly with
402 corresponding arterial SO₂ values as determined by pulse oximetry.

403 The imaging system and oximetry technique provides sufficient sensitivity to SO₂ such that it
404 may be applied to the study of a variety of disease models where hypoxia may be a factor. The
405 preliminary results presented in this paper suggest that any significant changes in SO₂ related to specific
406 pathological changes will be quantifiable, and it is hoped that future studies using this technique will
407 provide a deeper understanding of disease pathology. The oximetry algorithm developed may be easily
408 extended to a wide range of other applications in future where localised SO₂ measurement is required
409 *in vivo*, such as oximetry in rodent models of multiple sclerosis, rheumatoid arthritis and non-invasive
410 retinal oximetry in humans.

411

412

413 **Acknowledgment**

414 This work was funded by the University of Glasgow Sensors Initiative and the Lord Kelvin Adam Smith
415 scholarship programme.

416

417 **References**

418

419 Arango, J. M. a. M., 2009. Near-infrared spectroscopy as an index of brain and tissue oxygenation.
420 *British Journal of Anaesthesia*, Volume 103, pp. i3-i13.

421 Beach, J., 2014. Pathway to Retinal Oximetry. *Transl Vis Sci Technol*, 3(5).

422 Beach, J. et al., 1999. Oximetry of retinal vessels by dual-wavelength imaging: calibration and
423 influence of pigmentation. *Journal of Applied Physiology*, pp. 748-758.

424 Bosschaart, N. et al., 2014. A literature review and novel theoretical approach on the optical
425 properties of whole blood. *Lasers in Medical Science*, Volume 29, pp. 453-479.

426 Briely-Sabo, K. & Bjornerud, A., 2000. Accurate de-oxygenation of ex vivo whole blood using sodium
427 Dithionite. *Proc. Intl. Sot. Mag. Reson. Med*, Volume 8, p. 2025.

428 Cadotte, D. W. et al., 2012. Speckle variance optical coherence tomography of the rodent spinal
429 cord: in vivo feasibility. *Biomedical Optics Express*, 3(5), pp. 911-919.

430 Choudhary, T. R. et al., 2013. Assessment of acute mild hypoxia on retinal oxygen saturation using
431 snapshot retinal oximetry. *Investigative ophthalmology & visual science*, 54(12), pp. 7538-43.

432 Davies, A. L. et al., 2013. Neurological Deficits Caused by Tissue Hypoxia in neuroinflammatory
433 disease. *Annals of Neurology*, 74(6), pp. 815-825.

434 Denninghoff, K. & Smith, M., 2000. Optical model of the blood in large retinal vessels. *Journal of
435 Biomedical Optics*, 5(4), pp. 371-374.

436 Desai, R. et al., 2016. Cause and prevention of demyelination in a model multiple sclerosis lesion.
437 *Annals of Neurology*, 79(4), pp. 591-604.

- 438 Eltzschig, H. & Carmeliet, P., 2011. Hypoxia and Inflammation. *N Engl J Med*, Volume 364, pp. 656-
439 65.
- 440 Faber, D. J. et al., 2004. Oxygen Saturation-Dependent Absorption and Scattering of Blood. *Physics*
441 *Review Letters*, 93(2).
- 442 Figley, S. A. et al., 2013. A Spinal Cord Window Chamber Model for In Vivo Longitudinal Multimodal
443 Optical and Acoustic Imaging in a Murine Model. *PLOS one*, 8(3).
- 444 Friebel, M., Helfmann, J. & Meinke, M. C., 2010. Influence of osmolarity on the optical properties of
445 human erythrocytes. *J. Biomed. Opt.*, 15(5).
- 446 Ghassemi, P. et al., 2015. Rapid prototyping of biomimetic vascular phantoms for hyperspectral
447 reflectance imaging. *Journal of Biomedical Optics*, 20(12).
- 448 Hammer, M., Leistritz, S., Leistritz, L. & Schweitzer, D., 2001. Light Paths in Retinal Vessel Oxymetry.
449 *IEEE Transactions on Biomedical Engineering*, 48(5), pp. 592-598.
- 450 Hammer, M., Vilser, W., Riemer, T. & Schweitzer, D., 2008. Retinal vessel oximetry-calibration,
451 compensation for vessel diameter and fundus pigmentation, and reproducibility. *J. Biomed Opt.*,
452 13(5).
- 453 Johannssen, H. C. & Helmchen, F., 2010. In vivo Ca²⁺ imaging of dorsal horn neuronal populations in
454 mouse spinal cord. *The Journal of physiology*, 588(18), pp. 3397-3402.
- 455 Lesage, F., Brieb, N., Dubeaub, S. & Beaumont, E., 2009. Optical imaging of vascular and metabolic
456 responses in the lumbar spinal cord after T10 transection in rats. *Neuroscience letters*, 454(1), pp.
457 105-109.
- 458 MacKenzie, L., Choudhary, T., McNaught, A. & Harvey, A., 2016. In vivo oximetry of human bulbar
459 conjunctival and episcleral microvasculature using snapshot multispectral imaging. *Experimental Eye*
460 *Research*.
- 461 Mordant, D. et al., 2011. Spectral imaging of the retina. *Eye*, Volume 25, pp. 309-320.
- 462 Prael, S., 1999. Optical Absorption of Hemoglobin. *Oregon Medical Laser Center*,
463 <http://omlc.org/spectra/hemoglobin/index.html>.
- 464 Rodmell, P. et al., 2014. Light path-length distributions within the retina. *Journal of biomedical*
465 *optics*, 19(3).
- 466 Schweitzer, D. et al., 1995. Calibration-free measurement of the oxygen saturation in retinal vessels
467 of men. *Proc. SPIE, Ophthalmic Technologies V*, 2393(210).
- 468 Sharma, V. et al., 2011. Quantification of light reflectance spectroscopy and its application:
469 Determination of hemodynamics on the rat spinal cord and brain induced by electrical stimulation.
470 *NeuroImage*, 56(3), pp. 1316-1328.
- 471 Smith, M., 1999. Optimum wavelength combinations for retinal vessel oximetry. *Applied optics*,
472 38(1), pp. 258-67.
- 473 Smith, M. H., Denninghoff, K. R., Lompado, A. & Hillman, a. L. W., 2000. Effect of multiple light paths
474 on retinal vessel oximetry. *Applied Optics*, 39(7), pp. 1183-93.

A multispectral microscope for *in vivo* oximetry of rat dorsal spinal cord vasculature

- 475 Sorg, B. S. et al., 2005. Hyperspectral imaging of hemoglobin saturation in tumor microvasculature
476 and tumor hypoxia development. *Journal of biomedical optics*, 10(4).
- 477 Taylor, P. C. & Sivakumar, B., 2005. Hypoxia and angiogenesis in rheumatoid arthritis. *Current*
478 *opinion in rheumatology*, Volume 17, pp. 293-298.
- 479 Vinegoni, C., Lee, S., Feruglio, P. F. & Weissleder, R., 2014. Advanced Motion Compensation Methods
480 for Intravital Optical Microscopy. *IEEE Journal of Selected Topics in Quantum Electronics*, 20(2).
- 481 Yi, J. et al., 2015. Visible light optical coherence tomography measures retinal oxygen metabolic
482 response to systemic oxygenation. *Light: Science & Applications*, 4(e334).
- 483 Zijlstra, W., Buursmaa, A., Falke, H. & Catsburg, J., 1994. Spectrophotometry of hemoglobin:
484 absorption spectra of rat oxyhemoglobin, deoxyhemoglobin, carboxyhemoglobin, and
485 methemoglobin. *Comp. Biochem. Physiol.*, 107B(1), pp. 161-166.
- 486